Automated iterative neutrosophic lung segmentation for image analysis in thoracic computed tomography

Yanhui Guo,[a] Chuan Zhou, Heang-Ping Chan, Aamer Chughtai, Jun Wei, Lubomir M. Hadjiiski, and Ella A. Kazerooni
Department of Radiology, University of Michigan, Ann Arbor, Michigan 48109

(Received 8 June 2012; revised 9 June 2013; accepted for publication 12 June 2013; published 17 July 2013)

Purpose: Lung segmentation is a fundamental step in many image analysis applications for lung diseases and abnormalities in thoracic computed tomography (CT). The authors have previously developed a lung segmentation method based on expectation-maximization (EM) analysis and morphological operations (EMM) for our computer-aided detection (CAD) system for pulmonary embolism (PE) in CT pulmonary angiography (CTPA). However, due to the large variations in pathology that may be present in thoracic CT images, it is difficult to extract the lung regions accurately, especially when the lung parenchyma contains extensive lung diseases. The purpose of this study is to develop a new method that can provide accurate lung segmentation, including those affected by lung diseases.
Methods: An iterative neutrosophic lung segmentation (INLS) method was developed to improve the EMM segmentation utilizing the anatomic features of the ribs and lungs. The initial lung regions (ILRs) were extracted using our previously developed EMM method, in which the ribs were extracted using 3D hierarchical EM segmentation and the ribcage was constructed using morphological operations. Based on the anatomic features of ribs and lungs, the initial EMM segmentation was refined using INLS to obtain the final lung regions. In the INLS method, the anatomic features were mapped into a neutrosophic domain, and the neutrosophic operation was performed iteratively to refine the ILRs. With IRB approval, 5 and 58 CTPA scans were collected retrospectively and used as training and test sets, of which 2 and 34 cases had lung diseases, respectively. The lung regions manually outlined by an experienced thoracic radiologist were used as reference standard for performance evaluation of the automated lung segmentation. The percentage overlap area (POA), the Hausdorff distance (Hdist), and the average distance (AvgDist) of the lung boundaries relative to the reference standard were used as performance metrics.
Results: The proposed method achieved larger POAs and smaller distance errors than the EMM method. For the 58 test cases, the average POA, Hdist, and AvgDist were improved from 85.4 $\pm$ 18.4%, 22.6 $\pm$ 29.4 mm, and 3.5 $\pm$ 5.4 mm using EMM to 91.2 $\pm$ 6.7%, 16.0 $\pm$ 11.3 mm, and 2.5 $\pm$ 1.0 mm using INLS, respectively. The improvements were statistically significant ($p < 0.05$). To evaluate the accuracy of the INLS method in the identification of the lung boundaries affected by lung diseases, the authors separately analyzed the performance of the proposed method on the cases with versus without the lung diseases. The results showed that the cases without lung diseases were segmented more accurately than the cases with lung diseases by both the EMM and the INLS methods, but the INLS method achieved better performance than the EMM method in both cases.
Conclusions: The new INLS method utilizing the anatomic features of the rib and lung significantly improved the accuracy of lung segmentation, especially for the cases affected by lung diseases. *Improvement in lung segmentation will facilitate many image analysis tasks and CAD applications for lung diseases and abnormalities in thoracic CT, including automated PE detection.* © *2013 American Association of Physicists in Medicine*. [http://dx.doi.org/10.1118/1.4812679]

Key words: pulmonary embolism detection, lung segmentation, neutrosophic operation

1. INTRODUCTION

Computer-aided diagnosis and quantitative image analysis are major advantages in digital imaging. Quantitative evaluation and automated feature analysis provide useful information to clinicians for making diagnostic decisions, in addition to the qualitative assessment and conventional visual interpretation. Computerized image analysis includes many steps that depend on the imaging modality being analyzed as well as the applications and diseases of interest. In this study, we developed an automated lung segmentation method that can serve as a fundamental step for image analysis of various lung abnormalities in thoracic computed tomography (CT). Specifically, it will be the first step for our computer-aided detection system for pulmonary embolism (PE).

PE is a common, potentially fatal condition with high morbidity and mortality yet treatable disease.[1] PE can partially or completely occlude pulmonary arteries.[2,3] Usually thrombi form in the veins of the lower extremities or pelvis, and then travel into the pulmonary arteries. PE

leads to an estimated 50 000 deaths per year in the United States.[4]

PE diagnosis is based on clinical findings in combination with radiological studies. Computed tomography pulmonary angiography (CTPA) is a promising imaging modality for PE detection.[1,3] However, each CT scan for PE detection produces an average of about 300 axial images with a range of 200–600 slices. An increased number of examinations and images per CT examination result in prolonged reading time, which increases the radiologist's workload and fatigue. Reader fatigue is found to be a cause of decreased detection accuracy of PE and false negatives.[5] Computer-aided detection (CAD) is potentially a viable approach to assist radiologists in the detection of PE and reduce the chance of missing PEs.[3,5]

Automated segmentation of lung regions is a fundamental step in quantitative image analysis and CAD for PE in CTPA and other thoracic abnormalities such as lung nodules or interstitial diseases in CT. Because of the variations of patient positioning, lung volume and shape at different stages of a respiratory cycle, and in particular, in lungs containing lung diseases, lung segmentation remains a challenging task for automated image analysis.[6]

Several lung segmentation methods have been reported including thresholding,[7–11] classification,[12–14] registration,[15,16] and model-based[17] methods. Armato *et al.*[8] used a multiple gray level thresholding method to segment the lung regions followed by refinement of the thresholded regions on the 2D slices using the knowledge of lung structures. Hu *et al.*[7] developed an automated method to choose an optimal threshold based on the gray level characteristics in a specific data set. Sensakovic *et al.*[18] used a fixed intensity threshold to create lung parenchyma candidate regions. A concavity elimination algorithm and a modified directional gradient correlation filter were then used to obtain the final lung segmentation by removing the nonlung regions. Using two gray-level thresholds determined by histogram analysis, Armato *et al.*[19,20] developed a lung region segmentation method for automated lung nodule detection and analysis of pleural mesothelioma. Leader *et al.*[22] developed a heuristic threshold-based scheme for initial lung segmentation followed by a rule-based method to prune incorrectly segmented structures in the lung. These thresholding technique relies largely on the attenuation differences between the lung parenchyma and surrounding background, and tends to be unreliable when the lung contains abnormal regions, for example, a region of lung disease.[21]

Korfiatis *et al.*[14] employed K-means clustering followed by a hole-filling operation to obtain an initial lung region, and then an iterative support vector machine (SVM) neighborhood labeling method was used to identify the lung boundaries based on gray level and wavelet coefficient statistical features. Wang *et al.*[12] obtained an initial lung region estimation that included normal and mildly abnormal lung parenchyma based on CT values. The texture features at each pixel were calculated from the co-occurrence matrix and used to identify the abnormal lung regions that contained interstitial lung disease (ILD). The initial lungs and the identified abnormal lung regions were combined as the final lung segmentation. However, this method would fail when the lung contained severe ILD.

Arzhaeva *et al.*[16] and Rikxoort *et al.*[23] combined the thresholding technique and registration approach for lung segmentation. A multiatlas segmentation-by-registration approach (MAS) was applied to the CT scans where the thresholding approach failed to segment the lung region. Sluimer *et al.*[15,21] proposed a registration-based lung segmentation scheme, in which 15 CT scans with normal lungs were used as training set to build the masks of the normal lungs, and the masks were elastically registered to the test scans to identify the lung regions including those containing extensive diseases. The performance was evaluated in a small test set of only 10 cases. Li and Reinhardt[17] built a 3D statistical shape model based on the mean curvatures of lung in a training set. The model was then deformed iteratively by updating a snake for the refinement of the lung boundary. This method only considered normal scans and was not tested on lung scans with pathologies.

In clinical practice, many of the patients undergoing thoracic CT scans have lung diseases, making it difficult for an automated method to segment the lung regions accurately.[24] For accurate segmentation, the lung shape should be employed without depending solely on gray value information. Several methods have been reported to segment lung regions that contained lung diseases using the lung shape information. Sluimer *et al.* identified surrounding structures, such as the ribcage and the diaphragm, and combined those structures in a comprehensive segmentation scheme.[25] Prasad *et al.*[24] exploited the fact that the curvature of the ribs is closely matched to that of the lung boundary, and used a polynomial to approximate the curvatures of the ribs. A Bayes classifier was used to find the lung boundaries that had the optimal fitting to the polynomial model of rib curvatures. However, this approach was not applied to the whole lung volume, and it only segmented the middle region of the lungs on 2D slices.

We previously developed a lung segmentation method using expectation-maximization (EM) analysis in combination with morphological operations (EMM).[26] EM analysis was applied to the gray level histogram of the CT scan to estimate the threshold value for extraction of the lung regions. The rolling ball method[27] based on morphological operations was employed to connect the indentations where the arteries and veins enter and exit the lungs. However, the lung segmentation results were not accurate when the lung contained extensive diffused diseases, which are often present in patients with PE. In addition, PE detection methods developed for the aerated lung regions were not as effective in the diseased regions where the complex background structures could cause both false negatives (FNs) and false positives (FPs). A main motivation of this study is to improve PE detection by improving lung segmentation in the presence of lung diseases. If the diseased and the aerated regions in the lungs can be delineated, computer-vision techniques adaptive to the characteristics of the different structured background may be designed to reduce both FPs and FNs. In this study, we focused on the development of a novel method that utilized iterative neutrosophic operation and the rib anatomic information for

improvement of lung segmentation. The novelty of this method is that we take advantage of the flexibility of the neutrosophic logic operation which facilitates the combination of the structural properties of the image and other operations such as morphological filtering and edge detection, and the iterative approach allows further control of the process. To our knowledge, this is the first study that applies an iterative neutrosophic method to lung segmentation in volumetric CT images. The performance of the method was evaluated by comparison with the radiologist's manual segmentation as reference standard.

2. MATERIALS AND METHODS

2.A. Data sets

With the approval of Institutional Review Board (IRB), we selected 5 and 58 inpatient CTPA scans retrospectively from the patient files at the University of Michigan as training and testing set, respectively. The exams were performed with injection of low osmolar nonionic contrast of iodine. All five training cases were acquired with four-slice CT scanner. For the test set of 58 CTPA scans, 12, 8, and 38 scans were acquired with a 4-, 8-, and 16-slice CT scanner, respectively. The CT scanners were GE LightSpeed QX/I (17 cases), LightSpeed Ultra (8 cases), and LightSpeed16 (38 cases). The image acquisition techniques were 120 kVp (34 cases) and 140 kVp (29 cases), 300–600 mAs (397 ± 68 mAs), 3 mm collimation, 1.25 mm reconstruction slice thickness, and 0.625 mm reconstruction interval. The reconstruction kernels were STANDARD (56 cases) and SOFT (7 cases) with BODY filter for all 63 cases. The in-plane pixel size ranged from 0.506 to 0.977 mm with mean and standard deviation of 0.681 ± 0.071 mm. The 58 CTPA cases were diagnosed with positive PE during the patients' clinical care. An experienced thoracic radiologist provided reference standards for the lung regions by manually outlining the lung boundaries on the transverse views (slices) using a graphic user interface (GUI). For the lung boundaries containing lung diseases, the radiologist visually estimated the lung boundaries based on the anatomy of normal lung boundary. Figure 1 shows an example of radiologist's outline on a slice in which the right lung contained infection disease. Because manual drawing of the lung boundaries on every slice is very time consuming, the radiologist subjectively selected slices with significant lung shape changes, skipping a variable number of slices in between the selected slices, from the top to the bottom of the lung and drew the lung boundaries on these slices. An average of 15 ± 8 slices per CT scan, which corresponds to an average interval of 18.1 ± 9.6 mm, was selected by the radiologist. A total of 1144 slices were selected and the lung boundaries were manually outlined in the 58 test cases. Extensive lung parenchymal and/or pleural effusion diseases were identified by the radiologist in 34 of the 58 test scans and 2 of the 5 training scans. In the 34 cases with extensive diseases, 15, 9, 3, 3, 6, and 3 cases contained lung diseases of pleural effusions, emphysema, metastatic disease, pulmonary edema, atelectasis, and pneumonia, respectively. Of the manually outlined slices in these cases, 62, 46, 12, 12, 18, and 10 slices, respectively, intersected with the disease region. Note that five cases contained more than one type of diseases.

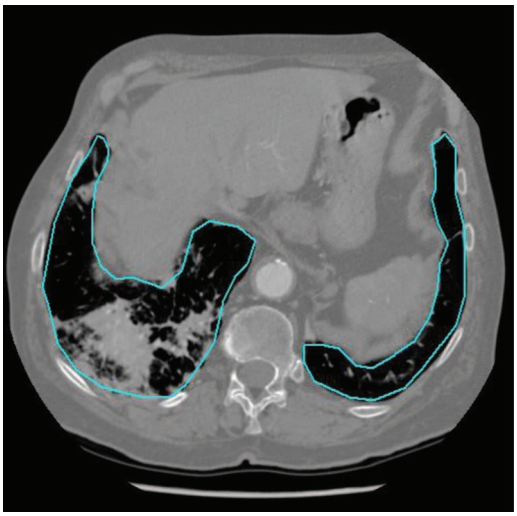

FIG. 1. An example of radiologist's outline as reference standard.

2.B. Methods

Our previously developed EMM method could not segment the lung region accurately in the cases with extensive lung diseases. Figure 2 shows examples of the lung segmentation by EMM in two cases, one had infection in the lung [Fig. 2(a)] and the other had pleural effusion [Fig. 2(b)]. The lung boundaries identified by EMM and the radiologist are shown in Figs. 2(c) and 2(d). It can be seen that the EMM method failed to segment the lung region accurately when the lung diseases separated the lung into several pieces or were connected to the pleura.

In this study, we developed an iterative neutrosophic lung segmentation (INLS) method to improve the EMM segmentation utilizing the anatomic features of the ribs and lungs. The ribs were extracted using a 3D hierarchical EM segmentation method. The ribcage was then constructed using morphological operations. Based on the anatomic features of the ribs and lungs, the initial EMM segmentation was refined to obtain the final lung regions using INLS. In the INLS method, the anatomic features were mapped into the neutrosophic domain, and the neutrosophic operation was performed iteratively to obtain accurate lung segmentation.

2.B.1. Ribcage construction

The ribcage is a reliable anatomic landmark in CT scan that surrounds the lung regions. Our previously developed EM-based rib segmentation method (EMRS) was adopted in this study for the segmentation of the rib structures.[6] All parameters for the EMRS method were kept the same as those previously trained with an independent lung nodule data set. To construct the ribcage, a 3D morphological dilation operation was applied to the EMRS segmented ribs to fill the gaps between the ribs using a cylindrical structuring element with the

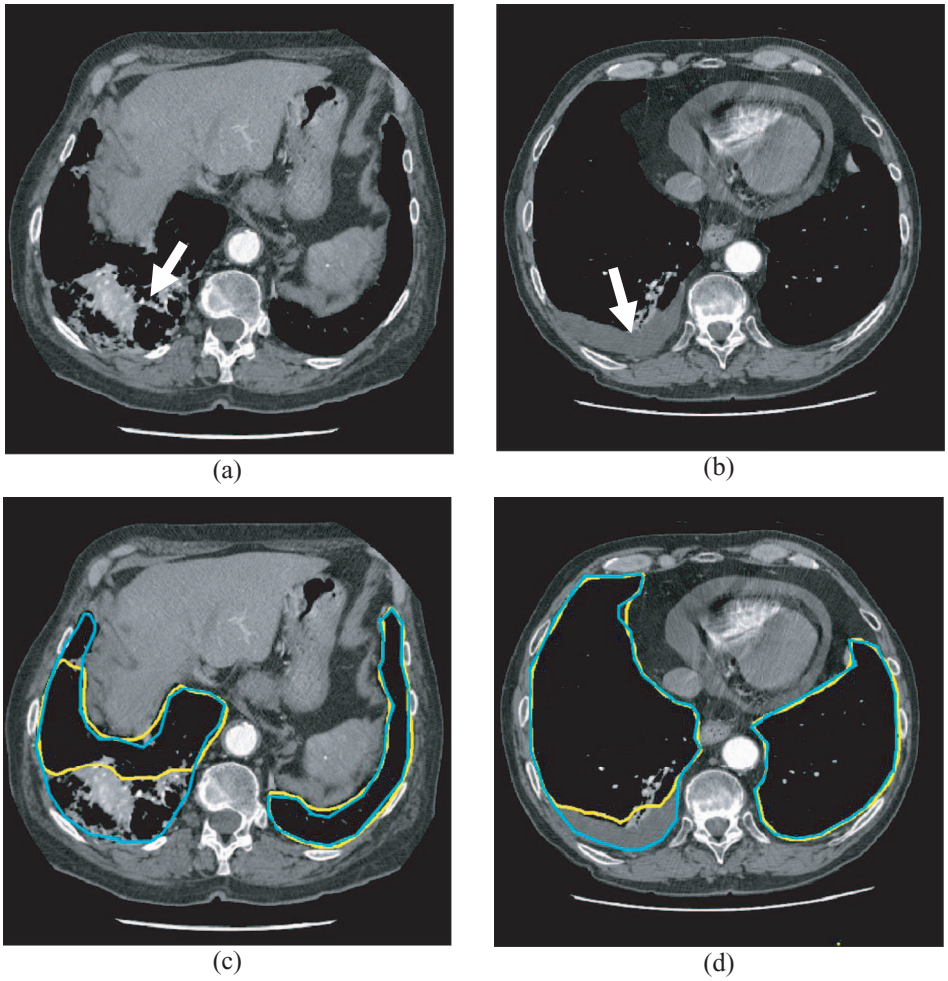

FIG. 2. Examples of lung segmentation by EMM method for two cases containing extensive lung diseases: (a) infection and (b) pleural effusion pointed by arrows. The lung boundaries identified by EMM is superimposed with radiologist's manual outline.

size of 1 × 1 × 37.5 mm (in x, y, and z direction). The size of the structuring element was chosen based on the anatomical knowledge that the gaps between human ribs would unlikely be larger than 35 mm. Although a larger structuring element could be chosen, it would cost longer computation time. Figure 3(a) shows an example of the 3D rendering of the EMRS segmented ribs and Fig. 3(b) shows the constructed ribcage after the gaps between the ribs were filled by the morphological dilation operation.

2.B.2. Lung segmentation using neutrosophic operation

In classical logic, a logical variable is restricted to the values of true (T) and false (F). As an extension of the classical logic set, the neutrosophic set (NS) (Ref. 28) adds a third logical value as an indeterminate value to address the uncertainties with more flexibility. In a neutrosophic set, every element x is described by an ordered triplet $x = (t, i, f)$, where t, i, and f are the degree of truth, indeterminacy, and falseness, respectively. In neutrosophic theory, T and F sets are used to represent the absolute true and absolute false sets, and I is for indeterminate or uncertain set. One of the advantages of using neutrosophy is that it can interpret true, false, and indeterminate set and the neutrosophic operations such as the logical AND, OR operation could be flexibly designed to reduce the indeterminacy of the whole set.[28]

Our previously developed EMM lung segmentation method was only designed to extract the air-filled lung regions with lower attenuation values. However, the lung regions not only contain air and vessels but also may contain lung diseases. Due to the relatively stable attenuation values of the air in the lungs and the ribs surrounding the lungs, the air region could be segmented by EMM and the ribs by the EMRS method, respectively. In INLS, the initial lung regions (ILRs) by EMM and the ribcage by EMRS were defined as the true neutrosophic sets, T_{EMM} and T_{Rib}, respectively. The magnitudes of the gradients in the rib enclosed region and ILR are defined as the indeterminacy set, I_{Rib} and I_{EMM}, respectively. Thus, the neutrosophic sets are defined as

$$A_{\mathrm{EMM}} = (T_{\mathrm{EMM}}, I_{\mathrm{EMM}}, F_{\mathrm{EMM}}), \quad (1)$$

$$A_{\mathrm{Rib}} = (T_{\mathrm{Rib}}, I_{\mathrm{Rib}}, F_{\mathrm{Rib}}), \quad (2)$$

where A_{EMM} and A_{Rib} are two neutrosophic sets representing the regions derived from ILR and the ribcage, respectively.

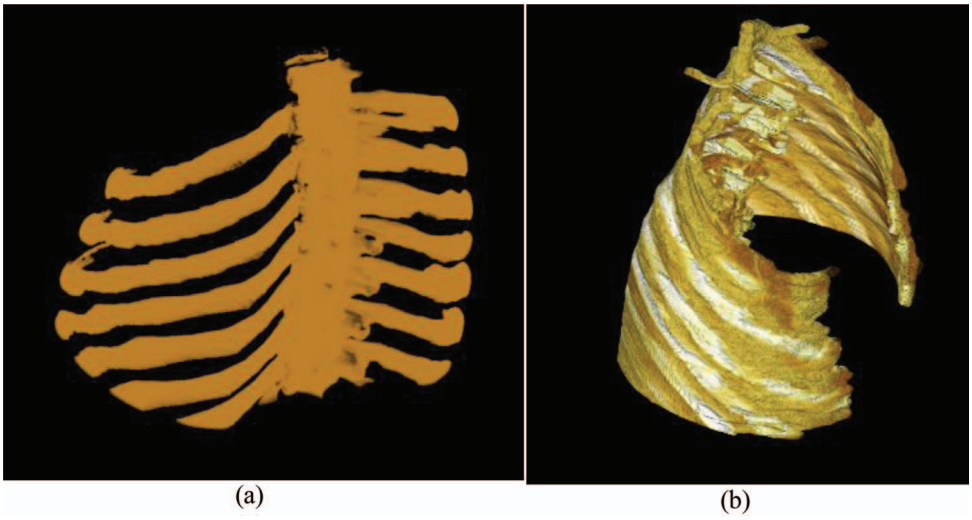

FIG. 3. An example of ribcage construction. (a) EMRS segmented ribs and (b) constructed ribcage.

F_{EMM} is the nonlung region beyond ILR and F_{Rib} is the region outside the ribcage. The anterior ribcage is not included in the A_{Rib} because the costal cartilages connecting the ribs to the sternum often cannot be segmented (see Fig. 3) and the anterior ribcage is in contact with the heart region.

For the situation that a lung contains lung disease, A_{Rib} may include the lung disease region and ribcage region, while A_{EMM} may exclude the lung disease region, therefore, both A_{EMM} and A_{Rib} are incorrect. To obtain an accurate lung region, an iterative process is performed in the NS domain to refine the A_{EMM} and A_{Rib} regions, as follows:

Initialization:

(1) T_{EMM} : the initial lung regions by EMM;
(2) $P_{T_{\text{EMM}}}$: a three-pixel-wide band along the boundaries of T_{EMM};
(3) $P_{T_{\text{Rib}}}$: a three-pixel-wide band along the boundaries of T_{Rib};
(4) $T_{\text{Rib}}^{(0)}$: the initial posterior ribcage region;
(5) I_{Rib}: the indeterminacy set consisting of the magnitude of the gradient in the ribcage region $T_{\text{Rib}}^{(0)}$;
(6) $I_{\text{Rib}}(\alpha)$: a subset of pixels in I_{Rib} whose gradient's magnitude is greater than α and labeled by binary values, $I_{\text{Rib}}(\alpha) = \begin{cases} 1 & I_{\text{Rib}} > \alpha \\ 0 & \text{otherwise} \end{cases}$, where α is a fixed threshold value for the normalized gradient magnitude of CT intensity determined by the training set. Because the gradient of lung boundary is much stronger than those of the air regions and tissue structures, the lung boundaries that can be extracted are not very sensitive to the variation between 0.1 and 0.3, α is therefore set to the middle value of 0.2.

Iterative process:

(1) At the ith iteration, the $I_{\text{Rib}}(\alpha)$ region is combined with $T_{\text{Rib}}^{(i)}$, $Y = T_{\text{Rib}}^{(i)} \cup I_{\text{Rib}}(\alpha)$.
(2) Perform morphological closing operation on Y: $Y' = (Y \oplus B_1) \ominus B_2$, where $\oplus$ and $\ominus$ denote the dilation and erosion with structuring elements B_1 and B_2 of sizes 3×3 and 5×5 pixels, respectively. Because the element size of erosion is larger than that of dilation, the boundary of the Y region will be peeled off.
(3) Obtain the new $T_{\text{Rib}}^{(i+1)}$: $T_{\text{Rib}}^{(i+1)} = Y'$.
(4) Calculate an indicator $W^{(i+1)} = \#(P_{T_{\text{EMM}}} \cap P_{T_{\text{Rib}}^{(i+1)}})$, where $P_{T_{\text{EMM}}}$ and $P_{T_{\text{Rib}}^{(i+1)}}$ are the sets of pixels in the three-pixel-wide bands along the boundaries of T_{EMM} and $T_{\text{Rib}}^{(i+1)}$, respectively. $\cap$ is the AND operation, and #() is a function to count the number of nonzero elements in the set. Therefore, $W^{(i+1)}$ is an integer counter that saves the number of pixels in the intersection between $P_{T_{\text{EMM}}}$ and $P_{T_{\text{Rib}}^{(i+1)}}$.
(5) Repeat the steps (1)–(4) until the maximum number of iterations is reached.

The iterative process continues until it reaches the maximum iteration, which is set as 20 in our experiments. For each iteration, the Y region will be peeled off by a two-pixel-thick layer (about 0.9 mm), thus a total of about 18 mm is peeled off after 20 iterations. Based on the knowledge of lung anatomy, the space between the ribs and the normal lung boundary usually does not exceed about 18 mm, therefore, the maximum iteration number of 20 will peel off enough layers of the ribcage to reach the true lung boundaries. The maximum of the set of the indicators $\{W^{(i)}, \text{i} = 1, \ldots, 20\}$ is then found and the index i^* of the iteration where $W^{(i)}$ reaches the maximum is identified. The maximum of $W^{(i)}$ indicates the best match between the outer contours of the i^*th iterative ribcage and the initial lung region by EMM. The final lung region $A_{\text{Seg}}{}^*$ is determined as the union of the ribcage set at the i^*th step and the initial EMM segmentation set.

$$i^* = \arg\max_i (W^{(i)}), \tag{3}$$

$$A_{\text{Seg}}^* = T_{\text{EMM}} \cup T_{\text{Rib}}^{(i^*)}. \tag{4}$$

Figure 4 illustrates the iterative process. Figure 4(a) shows the initial outlines of A_{EMM} and A_{Rib}. It demonstrates that the EMM segmented lung region T_{EMM} is smaller than the true

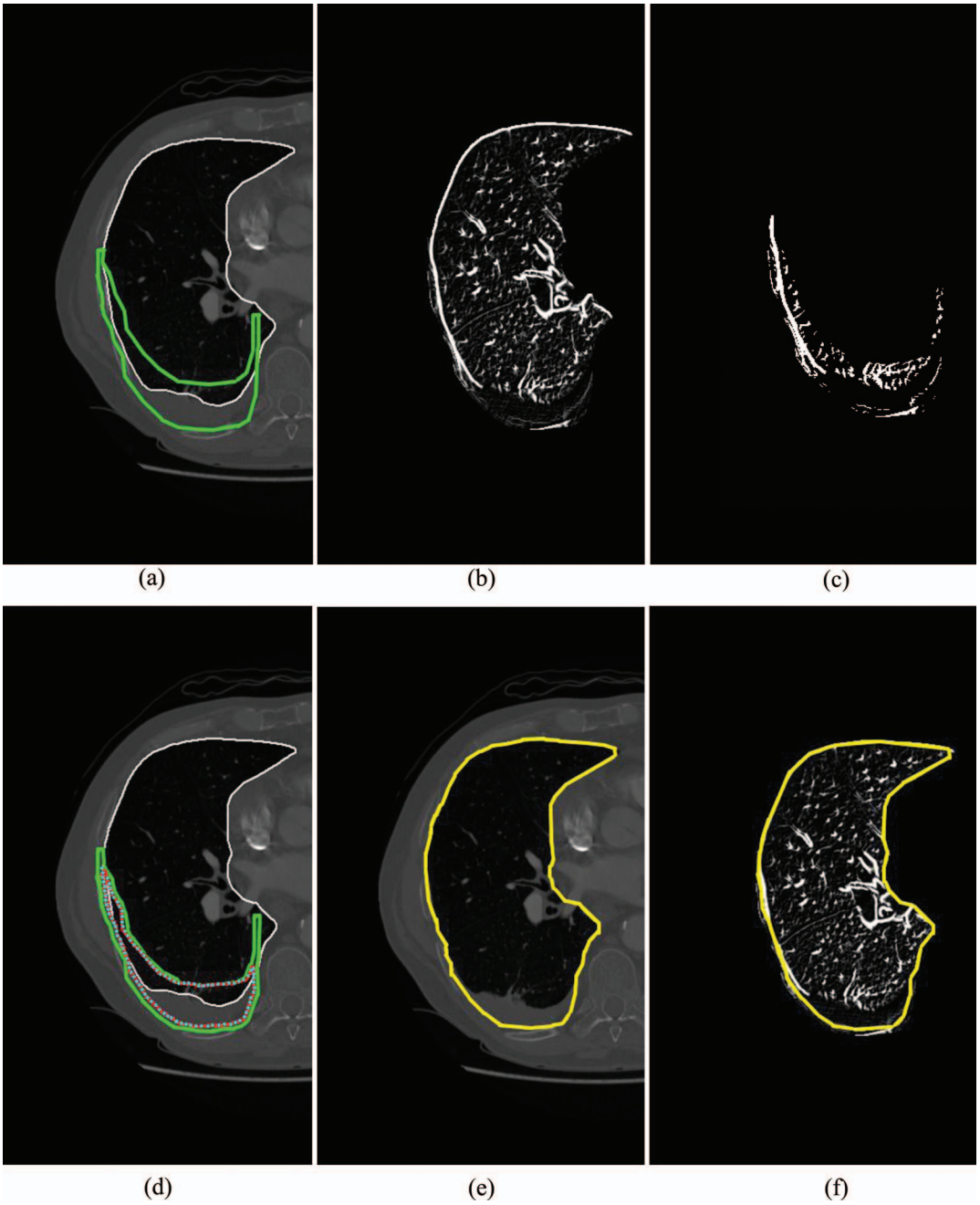

FIG. 4. Illustration of the INLS process. (a) Initial setting of the INLS, the EMM lung contour and the posterior part of the ribcage contours are shown in thin solid line and thick solid line, respectively. (b) The gray level gradient in the union of EMM lung segmentation and ribcage regions. (c) Thresholded gradients in the ribcage region. (d) Intermediate result at the fourth iteration showing the erosion of the ribcage (dotted line) and the contours of EMM segmentation (thin solid line) and initial ribcage (thick solid line). (e) Refined lung segmentation result. (f) The refined lung segmentation result on gradient image in (b).

lung region because of the pleural effusion, while the ribcage-guided segmentation $T_{\text{Rib}}^{(0)}$ includes the region with pleural effusion and ribcage. The upper boundary of the $T_{\text{Rib}}^{(0)}$ region is obtained by connecting the anterior of the ribcage segmented by EMRS (Fig. 3) and eroding with morphological operation to obtain a concave lung region. The exact location of this boundary is not critical because it does not affect the final lung boundary. Figure 4(b) shows the magnitudes of the gradients in the union of the ribcage region and the EMM segmented lung region. Figure 4(c) shows the thresholded gradient magnitude $I_{\text{Rib}}(\alpha)$ ($\alpha = 0.2$) within the ribcage region. It can be seen that the posterior lung boundaries are not clear and discontinued from the anterior part. Figure 4(d) shows an intermediate result at the fourth iteration, the updated ribcage outline moved toward the true lung boundaries. The final segmented lung boundary is shown superimposed on the original image [Fig. 4(e)] and the gradient image [Fig. 4(f)].

2.B.3. Performance evaluation

The lung boundaries manually outlined by an experienced radiologist on the transverse views were used as the

reference standard for the performance evaluation of our automated lung segmentation algorithm. Linear interpolation was performed to fill the gaps between the manually drawn sparse boundary points. Let $C = \{c_1, c_2, \ldots, c_p\}$ be the computer-identified lung boundary that contains p singly connected points, and $R = \{r_1, r_2, \ldots, r_q\}$ be radiologist's manually outlined and filled lung boundary that contains q singly connected points. The Euclidean distance between a computer-identified lung boundary point c_i and a reference standard point r_j is Dist(c_i, r_j), or equivalently, Dist(r_j,c_i). For each transverse view on which the radiologist manually outlined the lung boundaries, the accuracy of lung boundary detection is evaluated by three performance metrics:

(1) POA—also known as Jaccard similarity index:

$$\mathrm{POA}(C, R) = \frac{A_C \cap A_R}{A_C \cup A_R}, \tag{5}$$

where A_C and A_R are the computer segmented lung area and the reference standard lung area enclosed by the boundaries C and R. $\cup$ and $\cap$ are the union and intersection of two sets, respectively.

(2) Hausdorff distance between the boundaries C and R (Hdist)

$$\mathrm{Hdist} = \max\left\{\max_{c_i \in C}\{\min_{r_j \in R}\{Dist(c_i, r_j)\}\}, \max_{r_j \in R}\{\min_{c_i \in C}\{Dist(r_j, c_i)\}\}\right\}. \tag{6}$$

(3) Average distance between the boundaries C and R (AvgDist)

$$\mathrm{AvgDist} = \frac{1}{2}\left(\frac{1}{p}\sum_{i=1}^{p}\min_{r_j \in R}\{Dist(c_i, r_j)\} + \frac{1}{q}\sum_{j=1}^{q}\min_{c_i \in C}\{Dist(r_j, c_i)\}\right). \tag{7}$$

The distance measures are calculated in units of mm.

3. RESULTS

3.A. Average performance over all cases

Figure 5 shows examples of the segmented lung regions by the INLS method. Figure 5(a) shows a case without extensive lung diseases, Figs. 5(b) and 5(c) show cases having extensive diseases. The boundaries of lung segmentation results are marked using lines in different colors.

Because it is time consuming to manually outline the lung boundaries, the radiologist only outlined the lung boundaries on selected slices (transverse view). For the 58 test cases, the lung boundaries were manually outlined on a total of 1144 slices, which were used as the reference standard for performance evaluation. In comparison with radiologist's manual outlines, the performance metrics (POA, Hdist, and AvgDist) were calculated on the corresponding slices and the mean and standard deviation were computed over the 1144 slices. As shown in Table I, the mean and standard deviation of the POA, Hdist, and AvgDist were improved from 85.4 ± 18.4%, 22.6 ± 29.4 mm, and 3.5 ± 5.4 mm using EMM to 91.2 ± 6.7%, 16.0 ± 11.3 mm, and 2.5 ± 1.0 mm using INLS, respectively. The improvement is statistically significant ($p < 0.05$) for each performance metric by two-tailed Wilcoxon signed rank test. Figures 6(a)–6(c) show the cumulative percentage of slices having POA greater than a certain value and Hdist and AvgDist smaller than a certain value, respectively. It shows that 90.3% (1033/1144) of slices in the computer-segmented lungs had POA ≥ 85%, and that 82.1% (939/1144) and 99.8% (1141/1144) of slices in the computer-segmented lung boundaries had Hdist ≤ 25 mm and AvgDist ≤ 5 mm, respectively.

The run time of our INLS method including the rib segmentation and the EMM stages was estimated to be 1020 ± 241 s, on average, on a Dell Precision T3500 workstation with a 3.3 GHz Intel Xeon Processor.

3.B. Comparison in cases with and without extensive lung diseases

To evaluate the segmentation performance for the cases with and without extensive lung diseases, the 58 test cases were separated into two groups: 34 cases containing extensive lung diseases and 24 cases without extensive lung diseases. A 773 slices of the 34 cases and 371 slices of the 24 cases had radiologist's manually outlined lung boundaries. Table II shows the lung segmentation results for the cases with and without extensive lung diseases using the INLS and the EMM method. For both the EMM method and the INLS method, the average POA was higher and the Hdist and AvgDist were smaller for the cases without than those with extensive lung disease. For all cases, all three performance measures by the INLS method were significantly ($p < 0.05$) better than those by the EMM method.

Comparing the INLS method with the EMM method, the POA improved by 9.4% and 1.9% in the cases with and without diseases, respectively, and the Hdist and AvgDist improved by 30.6% and 36.6% in the cases with diseases, and by 24.8% and 8% in the cases without diseases, respectively. Furthermore, comparing the performance in the cases with and without diseases, the POA, Hdist, and AvgDist were degraded by only 1.5%, 64.3%, and 13.0%, respectively, by the INLS method, whereas they were degraded by 8.3%, 77.9%, and 64.0%, respectively, by the EMM method. The comparison demonstrates that the INLS method can achieve better performance both on the cases with and without diseases than the EMM method, and the INLS method is more robust against the presence of lung diseases than the EMM method for all three performance measures.

3.C. Comparison of segmentation of inner and outer lung boundaries

Along the lung boundaries, the arteries and veins entering and exiting the lungs and the heart are segmented as indentations. We refer to the portion of the lung boundaries

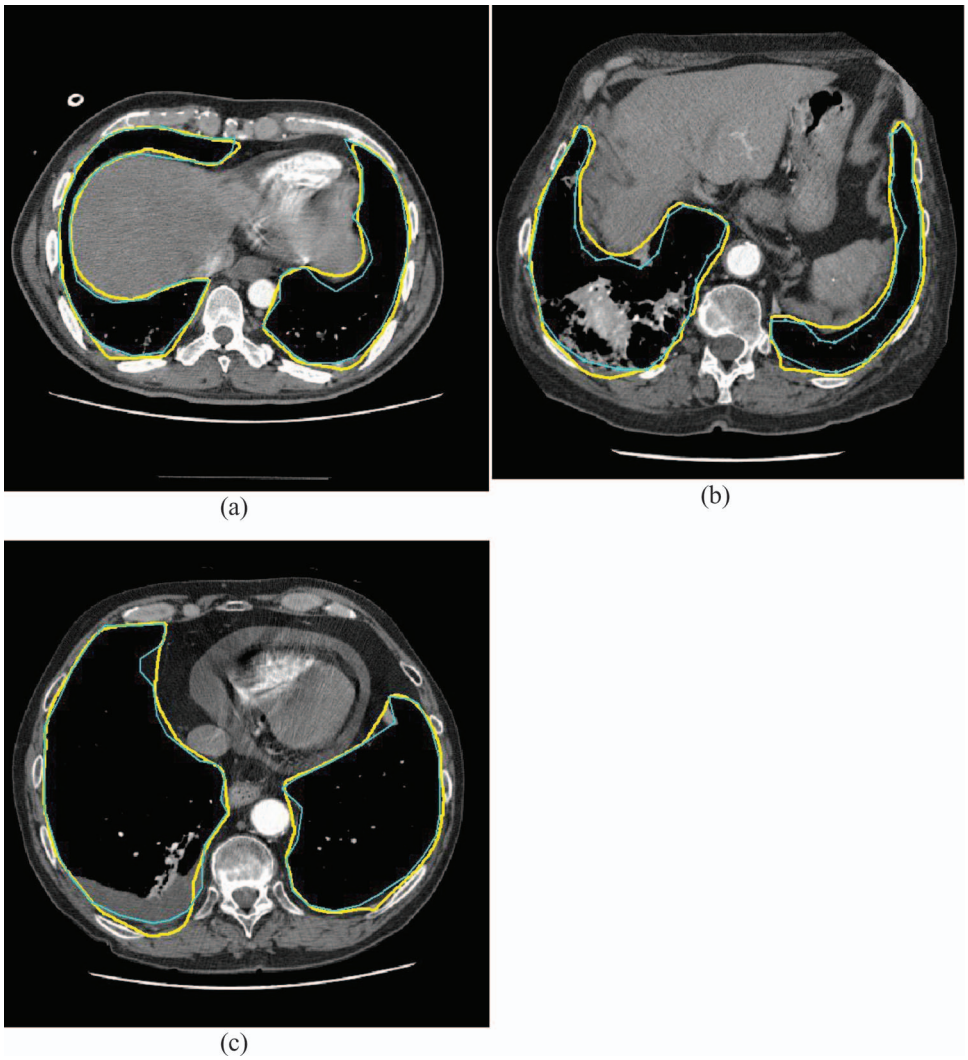

FIG. 5. Examples of segmentation result. The lung boundaries identified by INLS (yellow) is superimposed with radiologist's manual outline (cyan). (a) Case without extensive disease. (b) Case with infection. (c) Case with pleural effusion.

surrounding the heart as the inner boundaries and the remaining portions that are enclosed by the ribs and chest wall as outer boundaries, as shown in Fig. 7. Because the manual outlining of the inner boundaries depends on the radiologist's preferences with respect to the smoothness of boundary,[25] it remains unclear how to define the lung boundaries in the hilar area where the vessels enter and exit the lungs.

To evaluate the performance of INLS on the inner and outer boundaries, the computer-identified lung boundary C of each lung (left or right lung) was divided into inner boundary $InC = \{ic_1, ic_2, \ldots, ic_{pi}\}$ with pi points and outer boundary $OutC = \{oc_1, oc_2, \ldots, oc_{po}\}$ with po points, and radiologist's manually outlined lung boundary R has inner boundary $InR = \{ir_1, ir_2, \ldots, ir_{qi}\}$ with qi points and outer boundary $OutR = \{or_1, or_2, \ldots, or_{qo}\}$ with qo points, where $pi + po = p$ and $qi + qo = q$. The computer-identified lung boundary and the radiologist-drawn boundary were automatically divided on each slice at the extreme points of the top and bottom into inner and outer boundaries. Four performance metrics were used for the performance evaluation: Hausdorff distance of the inner boundary (InHdist), Hausdorff distance of the outer boundary (OutHdist), average distance of the inner boundary (InAvgDist), and average distance of the outer boundary (OutAvgDist). Table III shows the mean and standard deviation of InHdist, OutHdist, InAvgDist, and OutAvgDist for the INLS and EMM methods. The results show that the INLS method improved the EMM segmentation for both the inner and outer boundaries and the improvement in three of the four measures, InHdist, OutHdist, and InAvgDist, were statistically significant.

TABLE I. The performance of computer segmentation with reference to an experienced radiologist's manually drawn boundaries for the INLS and the EMM method. The p-values of the differences between the two methods are estimated by the two-tailed Wilcoxon signed rank test.

Method	POA (%)	Hdist (mm)	AvgDist (mm)
EMM	85.4 ± 18.4	22.6 ± 29.4	3.5 ± 5.4
INLS	91.2 ± 6.7	16.0 ± 11.3	2.5 ± 1.0
p-value	$<10^{-12}$	$<10^{-4}$	0.024

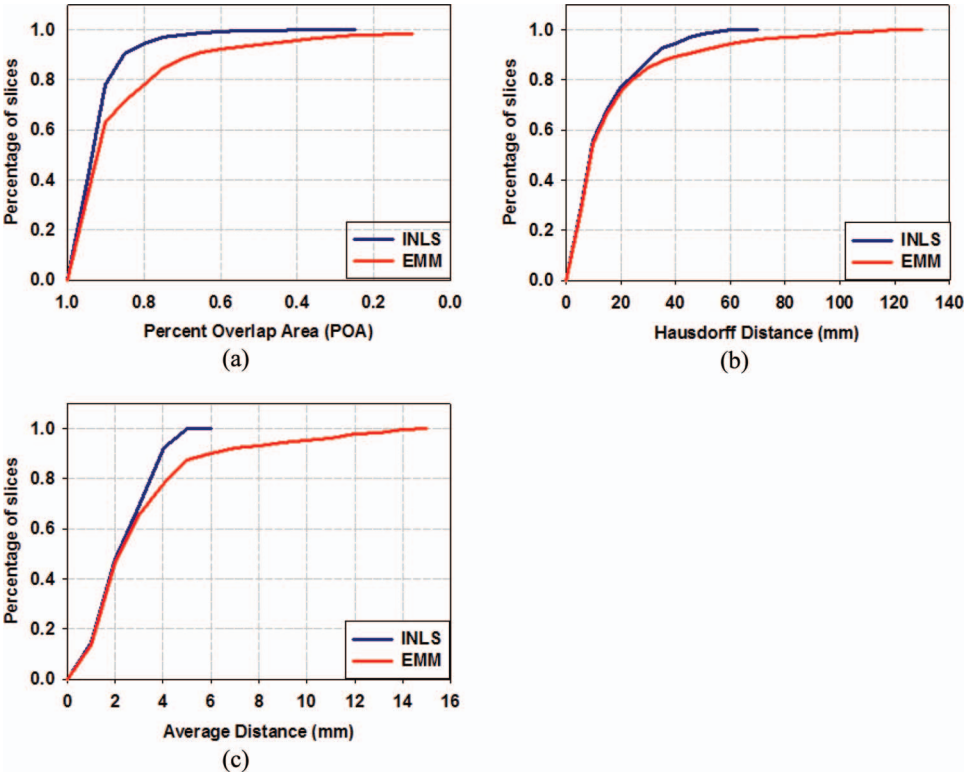

FIG. 6. Cumulative percentage of slices relative to the 1144 slices with radiologist's hand-drawn lung regions as reference standards, (a) having POA between the computer-segmented lung region and the reference standard greater than a certain value, and having (b) Hausdorff distance measure and (c) average Euclidean distance measure between the computer-segmented boundary and the reference standard smaller than a certain value.

Figure 8 shows the cumulative percentage of slices having distance measurements less than a certain value. The results show that both the EMM and INLS methods achieved better performance for the outer boundary than the inner boundary. For each metric, the INLS method reaches higher percentage than the EMM method. For example, 89.4% and 80.7% of the slices have InHdist less than 25 mm, while 97% and 84.4% of the slices have OutHdist less than 25 mm for INLS and EMM, respectively. Likewise, 96.4% and 80.8% of the slices have InAvgDist less than 5 mm, while 98.8% and 89.8% of the slices have OutAvgDist less than 5 mm for INLS and EMM, respectively.

TABLE II. The performance of computer segmentation with reference to an experienced radiologist's manually drawn boundaries for the INLS and the EMM method: with versus without extensive lung diseases.

	Method	POA (%)	Hdist (mm)	AvgDist (mm)
With diseases	EMM	82.9 ± 20.4	26.5 ± 31.1	4.1 ± 5.7
	INLS	90.7 ± 7.5	18.4 ± 12.1	2.6 ± 1.0
p-value[a]		$<10^{-15}$	$<10^{-10}$	$<10^{-3}$
Without diseases	EMM	90.4 ± 12.1	14.9 ± 24.3	2.5 ± 4.6
	INLS	92.1 ± 4.5	11.2 ± 7.6	2.3 ± 0.8
p-value[a]		$<10^{-4}$	$<10^{-9}$	$<10^{-8}$
With vs without diseases	EMM	$<10^{-10}$	$<10^{-20}$	$<10^{-13}$
p-value[b]	INLS	0.0225	$<10^{-27}$	$<10^{-7}$

[a]Two-tailed Wilcoxon signed rank test.
[b]Two-tailed Wilcoxon rank sum test.

4. DISCUSSION

Our previous studies[26] show that the EMM method is not reliable for segmenting the lungs containing extensive parenchymal or pleural lung diseases. It is difficult to segment the lungs with extensive lung diseases accurately if only the CT values and gradient information are used. In clinical settings, it is not uncommon that the CTPA exams for PE detection/diagnosis also contain extensive lung diseases. One of the advantages of our INLS method is that it utilizes the neutrosophic logic operations to combine the initial EMM lung segmentation, gradient, and anatomical information such as the ribcage. The novelty of the neutrosophic logic is the flexibility of the logic operation which facilitates the combination of the data and other operations such as morphological operations and edge detection.

The INLS method can work well in most cases with extensive lung diseases. Because it employs the ribcage as the landmark to recover the lung regions obstructed by extensive lung diseases, it is more effective in recovering the lung regions close to the ribs and less effective in the regions close to the sternum. In addition, if the entire lung is obstructed by severe extensive diseases and the CT attenuation values change substantially, the INLS method may not work well because the EMM method may fail to find a reasonable initial lung region and the ribcage cannot recover the entire lung region.

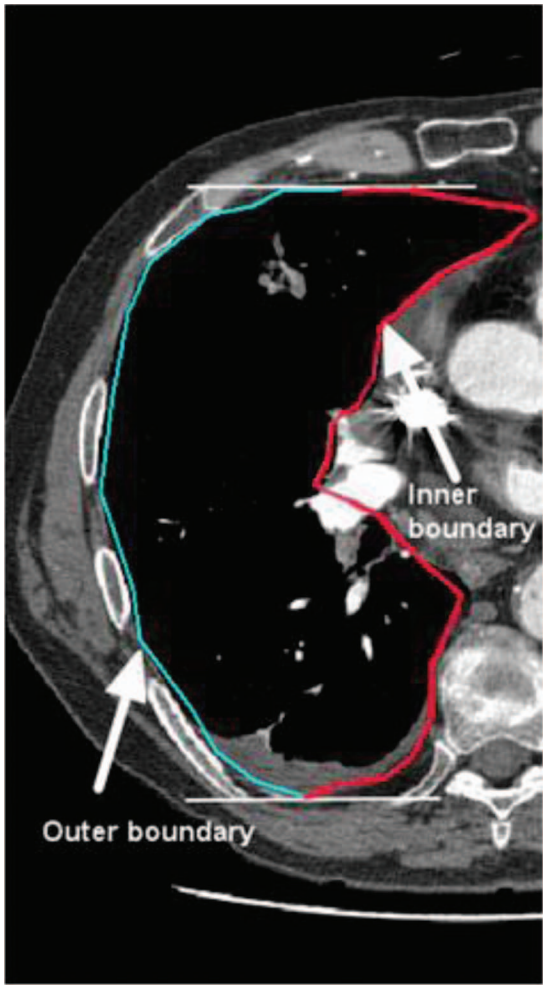

FIG. 7. Illustration of inner and outer boundaries.

Our analysis of the performance of the INLS method and the EMM method in the subsets of cases (with and without extensive lung diseases) and in different lung regions (inner versus outer) further verify the usefulness of the INLS method in overcoming the problems of lung segmentation in the presence of lung diseases. In lung regions in which the lung diseases corrupt the boundaries between the lung and the pleura and create an indeterminate region, the neutrosophic logic can be designed to recover the region as a part of the lungs based on some characteristic features. We found that the gradient information is useful for this purpose and improve the accuracy of lung segmentation significantly in the current data set. It is likely that other image characteristics such as texture features can also distinguish the diseased regions from normal lung tissues. The criteria to characterize the indeterminate regions will need to be designed based on the specific task of interest. The application of neutrosophic logic approach to other segmentation problems will warrant further investigations.

TABLE III. The performance of computer segmentation with reference to an experienced radiologist's manually drawn boundaries for the INLS and the EMM method: inner versus outer lung boundaries. The *p*-values of the differences between the two methods are estimated by the two-tailed Wilcoxon signed rank test.

Method	InHdist (mm)	OutHdist (mm)	InAvgDist (mm)	OutAvgDist (mm)
EMM	17.7 ± 23.2	14.4 ± 22.0	4.0 ± 5.7	3.2 ± 5.0
INLS	13.8 ± 12.0	7.4 ± 7.4	2.8 ± 1.4	2.2 ± 1.0
p-value	$<10^{-3}$	0.009	0.0121	0.2046

We used a data set of CTPA cases for evaluation of the lung segmentation methods because our primary goal is to accurately segment the lung regions for PE detection. However, it is expected that the developed method is applicable to thoracic CT exams for other types of lung abnormalities as an important step for image analysis and CAD applications. For example, because the INLS method can segment the total lung volume including the lung diseases while the EMM method mainly segment the aerated regions without diffused disease, the volume of the lung diseases can be estimated by subtracting the EMM segmented lung volume from the total lung volume. The quantitative and objective measure of the percentage of lung volume with disease will be clinically useful for radiologists to assess the severity of the lung diseases or to track the changes in severity over serial CT exams. Furthermore, the analysis of the feature characteristics in the diseased regions may provide additional information on the severity of the abnormality. For lung nodule detection, adaptive computer-vision techniques may be developed, taking into account the different background structures in the diseased and aerated regions, to improve lesion detection or FP reduction.

The limitation of our study is that the reference standard was provided by only one radiologist on the data set because it is time consuming to manually draw the lung boundaries.

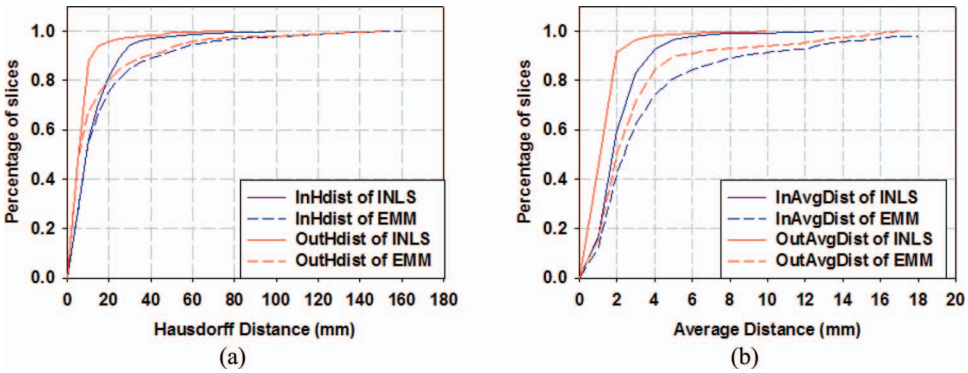

FIG. 8. Comparison of performances. (a) InHdist and OutHdist. (b) InAvgDist and OutAvgDist.

There is no evaluation of intra- and inter-reader variabilities. However, since the lung boundaries are relatively visible to the radiologist, inter- and intra-reader variabilities may be caused more by inconsistency in hand-drawing than judgment of the location of the boundaries. Furthermore, the improvement in segmentation by the INLS method is highly significant in most cases, it is not expected that the conclusion will change even if the variabilities are taken into account. Another limitation is that we have not evaluated the INLS method with cases containing invasive disease in the diaphragm and the chest wall. The method may not be able to segment the lung regions correctly if the intensity distributions of the diaphragm and the chest wall are changed substantially due to the presence of invasive disease. We will continue to improve the lung segmentation method for various disease conditions when representative cases are corrected into our database. We will also incorporate the improved lung segmentation method into our CAD system to improve PE detection in CTPA.

5. CONCLUSION

This study demonstrated that our new INLS method utilizing the anatomic information of rib structures and fusion with initial EMM segmentation improved the lung segmentation significantly compared with our previously developed EMM method, especially for the cases affected by lung diseases. Automated and accurate lung segmentation is a fundamental step for many image analysis tasks and CAD applications in thoracic CT including PE detection.

ACKNOWLEDGMENTS

This work is supported by USPHS Grant R01 HL092044.

[a]Author to whom correspondence should be addressed: School of Science and Technology, Saint Thomas University, Miami Gardens, Florida 33054. Electronic mail: yguo@stu.edu; Telephone: 734-936-9247; Fax: 734-615-5513.

[1]M. Rodger and P. S. Wells, "Diagnosis of pulmonary embolism," Thromb. Res. **103**, V225–V238 (2001).
[2]J. E. Dalen, "Pulmonary embolism: What have we learned since Virchow? - Natural history, pathophysiology, and diagnosis," Chest **122**, 1440–1456 (2002).
[3]U. J. Schoepf and P. Costello, "CT angiography for diagnosis of pulmonary embolism: State of the art," Radiology **230**, 329–337 (2004).
[4]F. A. Anderson, H. B. Wheeler, R. J. Goldberg, D. W. Hosmer, N. A. Patwardhan, B. Jovanovic, A. Forcier, and J. E. Dalen, "A population-based perspective of the hospital incidence and case-fatality rates of deep-vein thrombosis and pulmonary-embolism - The Worcester Dvt study," Arch. Intern Med. **151**, 933–938 (1991).
[5]Z. V. Maizlin, P. M. Vos, M. C. Godoy, and P. L. Cooperberg, "Computer-aided detection of pulmonary embolism on CT angiography: Initial experience," J. Thorac. Imaging **22**, 324–329 (2007).
[6]J. Z. Shi, B. Sahiner, H. P. Chan, L. Hadjiiski, C. Zhou, P. N. Cascade, N. Bogot, E. A. Kazerooni, Y. T. Wu, and J. Wei, "Pulmonary nodule registration in serial CT scans based on rib anatomy and nodule template matching," Med. Phys. **34**, 1336–1347 (2007).
[7]S. Y. Hu, E. A. Hoffman, and J. M. Reinhardt, "Automatic lung segmentation for accurate quantitation of volumetric X-ray CT images," IEEE Trans. Med. Imaging **20**, 490–498 (2001).
[8]S. G. Armato and W. F. Sensakovic, "Automated lung segmentation for thoracic CT: Impact on computer-aided diagnosis," Acad. Radiol. **11**, 1011–1021 (2004).
[9]Y. Masutani, H. MacMahon, and K. Doi, "Computer-assisted detection of pulmonary embolism," Proc. SPIE **3979**, 944–950 (2000).
[10]Y. Masutani, H. MacMahon, and K. Doi, "Automated segmentation and visualization of the pulmonary vascular tree in spiral CT angiography: An anatomy-oriented approach based on three-dimensional image analysis," J. Comput. Assist. Tomogr. **25**, 587–597 (2001).
[11]Y. Masutani, H. MacMahon, and K. Doi, "Computerized detection of pulmonary embolism in spiral CT angiography based on volumetric image analysis," IEEE Trans. Med. Imaging **21**, 1517–1523 (2002).
[12]J. H. Wang, F. Li, and Q. Li, "Automated segmentation of lungs with severe interstitial lung disease in CT," Med. Phys. **36**, 4592–4599 (2009).
[13]J. Wang, F. Li, K. Doi, and Q. Li, "A novel scheme for detection of diffuse lung disease in MDCT by use of statistical texture features," Proc. SPIE **7260**, 726039 (2009).
[14]P. Korfiatis, C. Kalogeropoulou, A. Karahaliou, A. Kazantzi, S. Skiadopoulos, and L. Costaridou, "Texture classification-based segmentation of lung affected by interstitial pneumonia in high-resolution CT," Med. Phys. **35**, 5290–5302 (2008).
[15]I. C. Sluimer, M. Niemeijer, and B. van Ginneken, "Lung field segmentation from thin-slice CT scans in presence of severe pathology," Proc. SPIE **5370**, 1447–1455 (2004).
[16]Y. Arzhaeva, M. Prokop, K. Murphy, E. M. van Rikxoort, P. A. de Jong, H. A. Gietema, M. A. Viergever, and B. van Ginneken, "Automated estimation of progression of interstitial lung disease in CT images," Med. Phys. **37**, 63–73 (2010).
[17]B. J. Li and J. M. Reinhardt, "Automatic generation of object shape models and their application to tomographic image segmentation," Proc. SPIE **4322**, 311–322 (2001).
[18]W. F. Sensakovic, S. G. Armato, C. Straus, R. Y. Roberts, P. Caligiuri, A. Starkey, and H. L. Kindler, "Computerized segmentation and measurement of malignant pleural mesothelioma," Med. Phys. **38**, 238–244 (2011).
[19]S. G. Armato and H. MacMahon, "Automated lung segmentation and computer-aided diagnosis for thoracic CT scans," Comput. Assist. Radiol. Surg. **1256**, 977–982 (2003).
[20]S. G. Armato, M. L. Giger, and H. MacMahon, "Automated lung segmentation in digitized posteroanterior chest radiographs," Acad. Radiol. **5**, 245–255 (1998).
[21]I. Sluimer, M. Prokop, and B. van Ginneken, "Toward automated segmentation of the pathological lung in CT," IEEE Trans. Med. Imaging **24**, 1025–1038 (2005).
[22]J. K. Leader, B. Zheng, R. M. Rogers, F. C. Sciurba, A. Perez, B. E. Chapman, S. Patel, C. R. Fuhrman, and D. Gur, "Automated lung segmentation in X-ray computed tomography: Development and evaluation of a heuristic threshold-based scheme," Acad. Radiol. **10**, 1224–1236 (2003).
[23]E. M. van Rikxoort, B. de Hoop, M. A. Viergever, M. Prokop, and B. van Ginneken, "Automatic lung segmentation from thoracic computed tomography scans using a hybrid approach with error detection," Med. Phys. **36**, 2934–2947 (2009).
[24]M. N. Prasad, M. S. Brown, S. Ahmad, F. Abtin, J. Allen, I. da Costa, H. J. Kim, M. F. McNitt-Gray, and J. G. Goldin, "Automatic segmentation of lung parenchyma based on curvature of ribs using HRCT images in scleroderma studies," Proc. SPIE **6915**, 69152K (2008).
[25]I. Sluimer, A. Schilham, M. Prokop, and B. van Ginneken, "Computer analysis of computed tomography scans of the lung: A survey," IEEE Trans. Med. Imaging **25**, 385–405 (2006).
[26]C. Zhou, H. P. Chan, B. Sahiner, L. M. Hadjiiski, A. Chughtai, S. Patel, J. Wei, P. N. Cascade, and E. A. Kazerooni, "Computer-aided detection of pulmonary embolism in computed tomographic pulmonary angiography (CTPA): Performance evaluation with independent data sets," Med. Phys. **36**, 3385–3396 (2009).
[27]S. R. Sternberg, "Biological image processing," Computer **16**, 22–34 (1983).
[28]F. Smarandache, *A Unifying Field in Logics: Neutrsophic Logic. Neutrosophy, Neutrosophic Set, Neutrosophic Probability* (American Research Press, Rehoboth, MA, 2005).